Unbounded two-dimensional wall turbulence induced by inverse cascade

Xi Chen ⬡,[*] Peng-Yu Duan ⬡, and Jianchao He ⬡

Key Laboratory of Fluid Mechanics of Ministry of Education, Beihang University
(Beijing University of Aeronautics and Astronautics), Beijing 100191, People's Republic of China

While seeking the ultimate statistical invariance of turbulence, classical boundary layer theory is unable to distinguish between the averaged states of wall flows with two-dimensional (2D) and three-dimensional (3D) fluctuations. Here we demonstrate glaring differences between 2D and 3D channel flows and present theoretical explanations for the differences in their Reynolds numbers' (Re_τ) asymptotic behaviors. In particular, due to the peculiar inverse cascade, large-scale wavy structures (LSWSs) are developed in 2D flows, which inject a high-energy flux toward the wall and cause extreme wall dissipation. The latter follows a distinct $Re_\tau^{1/3}$ scaling within the range covered by our direct numerical simulation ($130 < Re_\tau < 8100$). The same trend is also observed for the root mean square of the pressure and velocity fluctuations (as well as for the bulk velocity). Rationale for the scaling is further given through an LSWS-induced dissipative timescale (provided with the 2D friction law), which is unlike the viscous timescale in 3D flows due to the absence of LSWSs. As a counterpart to the classical boundary layer of bounded 3D fluctuations [Chen and Sreenivasan, J. Fluid Mech. **908**, R3 (2021); *ibid.* **933**, A20 (2022)], the results here reveal an unprecedented asymptotic state of wall flows in which the inverse cascade induces unbounded 2D fluctuations.

I. INTRODUCTION

Turbulent flows past solid boundaries experience strong shear and dissipate more energy at the wall than farther away [1]. Such flows are ubiquitous in nature and industrial applications, such as atmospheric boundary layers, oil passing through pipelines, and flows passing airborne. As they involve massive turbulence eddies transferring energy not only in spatial directions but also across length scales, characterizing turbulent flows is rather challenging [2,3]. Over the past century, seeking the statistical invariance of flows toward asymptotically high Reynolds numbers (Re_τ) has been one of the major issues in turbulence research [4,5]. As a milestone, in 1904 Prandtl proposed the boundary layer concept in which the viscous effect dominates the near-wall physics [4]. This insight gave birth to the celebrated *law of the wall* yielding Reynolds-number-invariant mean velocity profiles, based on which various turbulent models have been developed to predict turbulence fluctuations [5,6]. However, with the better resolved data accumulated in the past decades, notable Re_τ dependence has been observed for a series of fluctuations, calling the law of the wall into question [5–7]. On the other hand, as opposed to the well-known scenario of a forward cascade, the inverse cascade was realized in the 1960s [8,9] for two-dimensional (2D) turbulence, in which energy is transferred from small to large scales [10,11]. Later studies verified the inverse cascade in both numerical [12–14] and experimental [15–17] tests, mainly focusing on isotropic homogeneous turbulence and neglecting boundaries.

---

*chenxi97@outlook.com

As energy flux across scales has not generally been taken into account, the classical boundary layer theory has been unable to distinguish between wall flows with 2D and three-dimensional (3D) fluctuations. Pioneered by Kellay and Goldburg [18], gravity-driven soap-film experiments have been designed to investigate boundary effects in quasi-2D flows [19]. Later works [20–22] have revealed the missing link between energy flux and drag force, based on which a spectral theory has been developed enabling separate predictions of friction drag in 2D and 3D wall flows. Moreover, along with continuing interest in the mean velocity in 2D channels (2DCH) [23–25], there have been acute examinations of vorticity profiles [26] for a physical explanation of 2D friction law (explained in more detail later). However, little attention has been paid to fluctuations, which are the subject of the current article.

Recalling the Re_τ dependence of fluctuations in a 3D channel (and for pipe and flat-plate boundary layer flows), we have developed a defect law as [27,28]

$$\Phi_\infty - \Phi = \alpha_\Phi \mathrm{Re}_\tau^{-1/4}. \tag{1}$$

In Eq. (1), Φ represents wall-unit-scaled quantities including the wall values of dissipation rate, diffusion, root mean square (RMS) of pressure, and variances of wall shear stress and wall vorticity, etc. α_Φ is the proportionality coefficient and $\mathrm{Re}_\tau = u_\tau \delta/\nu$ is the friction Reynolds number, defined by the friction velocity u_τ, the half-channel height δ, and the viscosity ν. According to Eq. (1), a bounded state of near-wall turbulence is expected when $\mathrm{Re}_\tau \to \infty$, i.e., $\Phi \approx \Phi_\infty$, and hence the law of the wall is recovered [7].

Here we report that in 2DCH the fluctuations introduced above all follow a different power-law scaling,

$$\Phi = \beta_\Phi \mathrm{Re}_\tau^{1/3}, \tag{2}$$

where β_Φ is the proportionality coefficient. In contrast to Eq. (1), an unbounded growth of Φ is implied by Eq. (2) with increasing Re_τ. Accordingly, the current article not only establishes scaling laws for 2D fluctuations (hence prompting the verification in soap-film experiments), but also sheds light on the debate between the defect law [27,28] and the logarithmic law [29–32] in 3D wall flows.

II. RESULTS AND ANALYSIS

Via direct numerical simulation (DNS) of the 2D Navier-Stokes equations using our own finite-differential code [33], we present 16 cases of well-resolved 2DCH in the domain $L_x \times L_y = 8\delta \times 2\delta$ for Re_τ from 130 to 8100, and three long channel cases with $L_x \times L_y = 24\delta \times 2\delta$ for double confirmation of our findings. When converted to bulk Reynolds number $\mathrm{Re} = U_b \delta/\nu$ with U_b the bulk velocity, our flows span almost three decades, $3 \times 10^3 < \mathrm{Re} < 10^6$, with the highest Re about five times larger than ever treated before [26] [Fig. 1(a)]. Experimental (EXP) data for quasi-2D soap films [20,21] are included for comparison. Also, the current data sets provide a benchmark for the comparison with 3D channels (3DCH) by Ref. [34] for Re_τ from 180 to 5200.

The details of our DNS settings are described in Appendix A. Hereafter, we use the notation $\langle \cdot \rangle$ to indicate the mean value of a quantity, for which time-streamwise and flip-over averaging with respect to the centerline are performed (along with spanwise averaging for 3D flows). As such, the moderate asymmetry near the centerline noted in Ref. [25] is ignored as we focus on the wall or maximum values far from the center. Moreover, the streamwise (x) and wall-normal (y) fluctuation velocities are represented as u and v, respectively, with U indicating the streamwise mean velocity. The superscript "+" indicates normalization by viscous or wall units of u_τ and $\ell_\tau = \nu/u_\tau$, and the superscript prime indicates the RMS.

As shown in Fig. 1(b), wall values of the turbulent dissipation rate ϵ_w^+ and the RMS of pressure fluctuation $p_w'^+$ in 2DCH follow the same $\mathrm{Re}_\tau^{1/3}$ scaling as in Eq. (2). The displayed Re_τ ranges from about 10^2 to 10^4, covering both the stable-traveling-wave regime and the strongly fluctuating regime as reported in Ref. [26]. The latter work demarcates the two regimes by a critical $\mathrm{Re}_\tau \approx 530$. This transition is also discerned in our data of ϵ_w^+ through a modest hump at $\mathrm{Re}_\tau \approx 600$ [beyond which
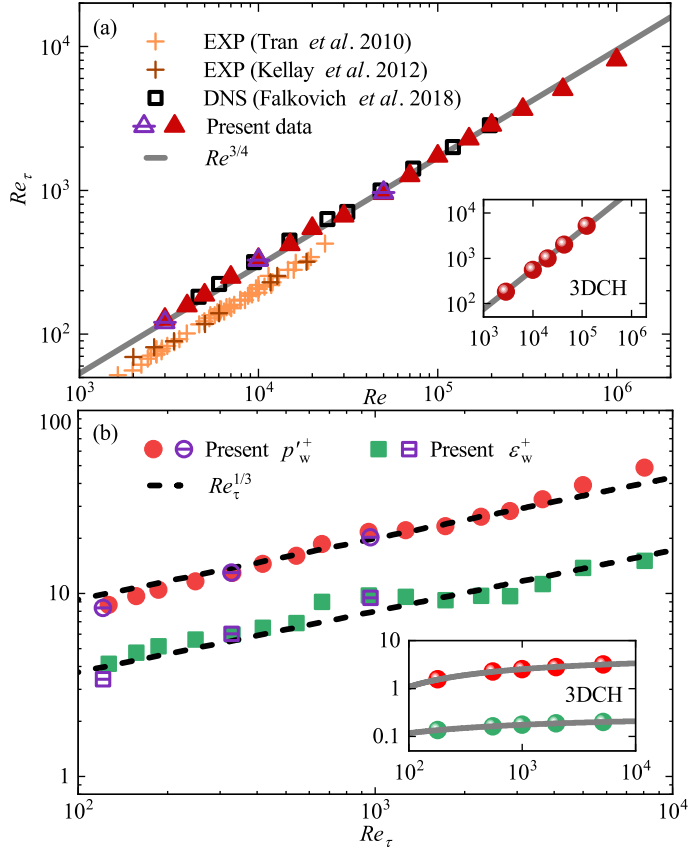
FIG. 1. (a) Re_τ vs Re in 2DCH. The solid line represents $Re^{3/4}$ resulting from the 2D friction law [20,26], as explained in the text. Inset: The same plot for 3DCH, where the solid line indicates $Re^{0.88}$ (see Ref. [3]). (b) Re_τ variations for ϵ_w^+ (squares) and $p_w'^+$ (circles), where the dashed lines represent Eq. (2). Inset: ϵ_w^+ (green) and $p_w'^+$ (red) in 3DCH with the solid lines representing Eq. (1). In all the plots, crosses indicate quasi-2D experiments [20,21], and the others are DNS. The 3DCH data are from Ref. [34], while our 2DCH data are marked as solid symbols (for $L_x = 8\delta$) and open symbols with bars (for $L_x = 24\delta$).

ϵ_w^+ reverts to Eq. (2) again]. However, $p_w'^+$ is rather smooth and closely adheres to Eq. (2) for the whole Re_τ range. Note that due to the nonslip wall condition, $\epsilon_w \equiv \langle\nu|\nabla u|^2|\rangle|_{y=0} = \langle\nu(\partial_y u)^2\rangle|_{y=0}$, and hence $\epsilon_w^+ = (\tau_w'^+)^2 = (\Omega_w'^+)^2$, where τ_w' is the RMS of the wall shear stress and Ω_w' is the RMS of the wall vorticity.

On the other hand [Fig. 1(b) inset], the streamwise dissipation ϵ_w^+ and pressure RMS $p_w'^+$ in 3DCH are about ten times smaller at a similar Re_τ, and following Eq. (1), they saturate to bounded values of $\epsilon_{w,\infty}^+ = 1/4$ and $p_{w,\infty}'^+ = 4.4$, respectively. This is very surprising because it is harder to generate steady turbulence in 2DCH, and hence less turbulence is expected, but the data show just the opposite. Understanding what causes such a glaring difference between 2D and 3D flows may substantially widen our fundamental perspective on wall turbulence.

In fact, prominent large-scale wavy structures (LSWSs) are developed occupying almost the entire wall-normal region of the 2D channel [Fig. 2(a)], as was also observed in Ref. [26]. The LSWSs, corresponding to the streamwise wavelength of about 4δ (or the wave number $k_x\delta = \pi/2$), are further found to be generated by pairs of large-scale antiswirling vortices (the "engine" of the LSWSs), sitting on the bottom and top walls [Fig. 2(b)], entraining high-momentum fluids from the center and injecting them toward the wall. Under such empowered injections, extreme dissipation
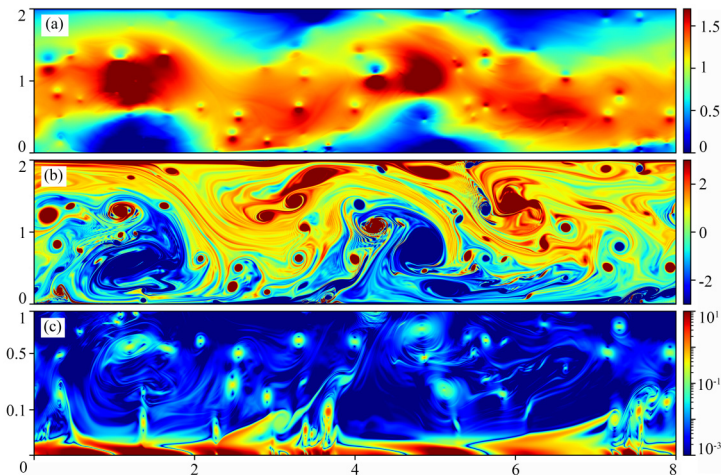
FIG. 2. Snapshots of (a) the streamwise velocity, (b) the voricity normalized by U_b and δ, and (c) the turbulent dissipation rate normalized by viscous units. Abscissas indicate the streamwise flow domain; ordinates left indicate the wall-normal ranges, and right are the color bars. Note that in (c), the left ordinate extends from the bottom wall to the centerline via $\sqrt{y/\delta}$ for a clearer view near the wall. Data are taken from our DNS at $Re_\tau \approx 2000$.

occurs in the vicinity of the wall [Fig. 2(c)] due to the intensive strain rate. In contrast, due to the absence of antivortex pairs, outer structures in 3DCH are not as energetic as the LSWSs in penetrating the near-wall region (see Appendix D and the Supplemental Material for movies [35]), though moderate modulations exist [36]. Therefore, the inner and outer flows have less interplay in 3DCH than in 2DCH, so viscous units are the exclusive metrics for near-wall physics under which growing 3D fluctuations are asymptotically invariant as per Eq. (1).

Moreover, in 3DCH, there is a celebrated von Kármán log-law region where the viscous scale separates from the outer flow scale [37]. However, due to the LSWSs, the inner and outer dynamics are highly coupled in 2DCH, so there is no basis for scale separation. The latter analysis is entirely consistent with Fig. 3(a) in that there is barely a log law in 2DCH. Even if a fit of $U^+(y^+)$ is
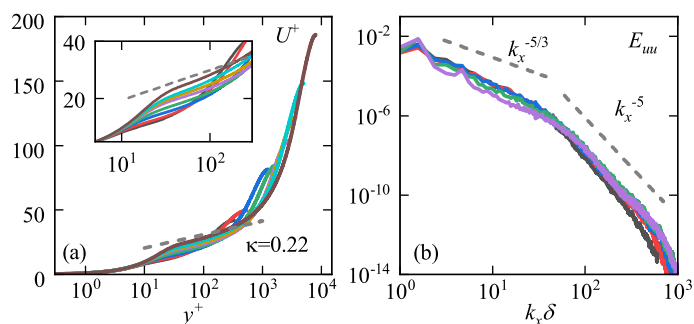

FIG. 3. (a) Wall-normal dependence of the streamwise mean velocity normalized by viscous units. The nominal logarithmic slope of $\kappa = 0.22$ is marked by a dashed line, but the intercept changes dramatically with Re_τ (see the inset for a zoomed-in view). Solid lines are our 2DCH DNS data for Re_τ from 330 to 8100. (b) Spectra of E_{uu} varying with the wave number k_x (normalized by the half-channel height δ) in 2DCH for Re_τ from 1720 to 8100. Dashed lines indicate $k_x^{-5/3}$ and k_x^{-5} spectra, both of which were observed in quasi-2D experiments in Ref. [17].
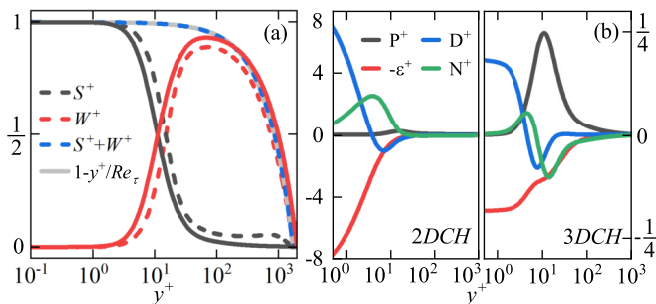
FIG. 4. (a) Momentum budget of Eq. (3): solid lines for 3D and dashed lines for 2D channels. (b) Kinetic energy budget of Eq. (4): left for 2D and right for 3D channels. Lines are DNS data at similar Reynolds numbers $Re_\tau \approx 2000$, with colors representing different terms marked in the legends.

performed by a logarithmic function with the seemingly like slope $\kappa = 0.22$, the intercept changes dramatically with different Re_τ values [Fig. 3(a) inset], hence breaking the log law. A further comparison between our 2DCH and soap-film experiments [24] is given in Appendix F, where the mean velocity data of the quasi-2D case lies between the 2D and 3D channels. This observation marks a vital difference between 2DCH and 3DCH, a significant point that we will come back to later.

In a way reminiscent of 2D homogeneous isotropic turbulence, as there is no vortex stretching, energy can be transferred from small to large scales and leads to energy condensation consisting of large-scale vortex pairs [16,38–40]. Such an inverse cascade is indicated by the $k_x^{-5/3}$ velocity spectrum [41], which is indeed observed from our centerline velocity shown in Fig. 3(b). Therefore, the data suggest the 2D scenario that an inverse cascade [Fig. 3(b)] induces antivortex pairs [Fig. 2(b)], which further lead to LSWSs [Fig. 2(a)] that completely alter the classical boundary layer.

We also note the forward enstrophy cascade [25,42,43] developed in 2DCH, as shown by the k_x^{-5} spectrum at smaller scales for $k_x \delta > 10^2$ in Fig. 3(b). Such a two-power-law spectrum has been identified in many previous works, e.g., in quasi-2D experiments of thin fluid layers driven by an electromagnetic force [16,17,39]. Moreover, the steeper slope of the -5 spectrum compared with the derived -3 spectrum [41] might be due to the presence of viscous dissipation and large-scale long-lived vortices, as was also speculated in Ref. [17]. In fact, whether there appears a single cascade or the coexistence of two cascades is determined by many factors including how the turbulence is triggered and sustained, as discussed in previous experiments [21,24,40,43] and simulations [13,14,22]. Here, for channel flows, the pressure gradient injects energy while dissipation damps out energy by most at walls. Competition between the two might cause the coexistence of two cascades. Even so, we stress the effect of the inverse energy cascade, as both the antivortex pairs and LSWSs focused on here are at large scales, far from the small-scale enstrophy cascade regime in Fig. 3(b).

The energy transfer in the wall-normal direction is now further examined. At first, the mean momentum balance in 2DCH [23] is the same as in 3DCH [Fig. 4(a)],

$$S^+ + W^+ = 1 - y^+/Re_\tau, \tag{3}$$

where $S^+ = \partial U^+/\partial y^+$ is the mean shear and $W^+ = -\langle uv \rangle^+$ is the Reynolds stress. Since $S^+ + W^+ \approx 1$ near the wall, crossing $S^+ = W^+$ (Fig. 4(a)) yields the maximum production $P_\infty^+ = 1/4$, which is valid for both 2D and 3D channels. However, vital differences are observed for $\langle uu \rangle$ budget (Fig. 4(b)),

$$P^+ + D^+ + N^+ = \epsilon^+, \tag{4}$$

where in addition to P^+ and ϵ^+, D^+ is diffusion and N^+ is the nonlinear effect of pressure strain and turbulent convection, for which explicit expressions are given in Appendix B.

Specifically, while there is a common balance between dissipation and diffusion toward the wall, their magnitudes are much larger in 2DCH than in 3DCH. As shown on the right-hand side of Fig. 4(b), there is a slight imbalance between the wall dissipation and maximum production in 3DCH, and with increasing Re_τ, their tendency to eventually balance each other inspired us to postulate Eq. (1) [27,28]. In contrast, the left-hand side of Fig. 4(b) shows that in 2DCH, production is no longer the dominant energy supplier, as N^+ overtakes it by transferring a huge amount of energy toward the wall that is eventually damped out by dissipation. This is entirely in line with the large-scale vortex pairs in Fig. 2(b), where swirls and entrainments can induce dramatic pressure strain and turbulent convection, both of which contribute to N^+ substantially. Note that the lack of vortex pairs in 3DCH (see Supplemental Material, Movie (b) [35]) also explains the relatively mild variation of N^+ on the right-hand side of Fig. 4(b), because of the gentle pressure strain and convection.

III. THEORY FOR THE SCALING

The rationale behind the observed $\mathrm{Re}_\tau^{1/3}$ scaling in 2DCH has now been developed. Starting with the wall dissipation ϵ_w, it basically corresponds to the energy scaled by u_τ^2 being dissipated over a certain timescale t_w (to be determined). If in viscous units, $t_w \sim \ell_\tau/u_\tau$, then $\epsilon_w \sim u_\tau^4/\nu$, which means the bounded $\epsilon_w^+ \sim O(1)$, as indicated by Eq. (1) for 3DCH. However, in 2DCH, as the high momentum of the LSWS penetrates toward the wall, the true dissipative time should be smaller than the viscous time ℓ_τ/u_τ. We thus estimate $t_w \sim \ell_\tau/U_b$ [44], which gives rise to $\epsilon_w \sim u_\tau^2/(\ell_\tau/U_b)$, and hence

$$\epsilon_w^+ \sim U_b/u_\tau. \tag{5}$$

As this stage, recall the 2D friction law $f \equiv u_\tau^2/U_b^2 \sim \mathrm{Re}^{-1/2}$ (see, e.g., Ref. [20]), which, according to the definitions $\mathrm{Re}_\tau = u_\tau\delta/\nu$ and $\mathrm{Re} = U_b\delta/\nu$, is equivalent to

$$\mathrm{Re}_\tau \sim \mathrm{Re}^{3/4}, \tag{6}$$

$$U_b/u_\tau \sim \mathrm{Re}_\tau^{1/3}. \tag{7}$$

Combining Eq. (5) and Eq. (7), we obtain Eq. (2) for ϵ_w^+, and hence the wall diffusion $D_w^+ (= \epsilon_w^+)$ and pressure $p_w'^+$.

Note that the above 2D friction law was first obtained from spectrum consideration [13,20,21], and later derived again by estimating the mean pressure gradient via $\nu_e U_b/\delta^2$, where $\nu_e \sim \sqrt{\nu U_b \delta}$ is the effective eddy viscosity [26]. In Fig. 1(a) Eq. (6) is well justified by our data. Also, the agreement between the data of Ref. [26] and ours validates the accuracy of our simulation. In Fig. 5 we verify that Eq. (7) once again shows good agreement.

As a comment, when invoking the log law $U_b/u_\tau \propto \ln \mathrm{Re}_\tau$ instead of Eq. (7), from Eq. (5) one obtains

$$\Phi = A_\Phi \ln \mathrm{Re}_\tau + B_\Phi, \tag{8}$$

where Φ indicates ϵ_w^+ (and other aforementioned quantities) with A_Φ and B_Φ coefficients. However, as shown and explained in Fig. 3(a), the log law is nullified by LSWS, resulting in the failure of Eq. (8) in 2DCH. It is worth noting that in the context of the competition between Eq. (1) and Eq. (8) for 3D wall flows [29–32], the newly obtained Eq. (2) is indeed valuable. The latter equation implies that the unbounded growth of fluctuations in 3DCH is unlikely due to the absence of vortex condensation.

Finally, we draw attention to the RMS peak of the streamwise velocity, i.e., $u_p'^+$. Unlike that located near the wall in 3DCH, the peak in 2DCH is at about $y/\delta \approx 0.25$ (Appendix C). This indicates that the peak is essentially an outer flow quantity, and $u_p'^+$ should scale as U_b^+ and follow
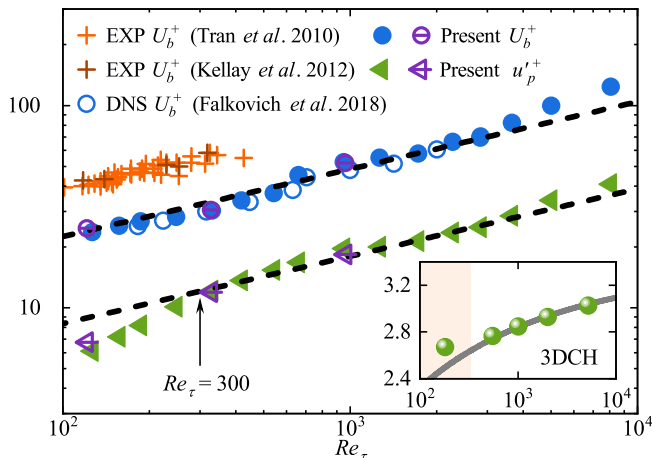
FIG. 5. Bulk velocity U_b^+ and peak of the streamwise velocity fluctuation $u_p'^+$ follow the same $\mathrm{Re}_\tau^{1/3}$ scaling (dashed lines) in 2DCH. Inset: $u_p'^+$ in 3DCH with the solid line resulting from Eq. (1). Data origins are the same as in Fig. 1. Note the arrow in the figure and the shaded region in the inset, both of which mark data deviation for $\mathrm{Re}_\tau \leqslant 300$.

the same $\mathrm{Re}_\tau^{1/3}$ scaling in Eq. (7), as is indeed verified by Fig. 5. In contrast, the inset shows $u_p'^+$ in 3DCH, a bending trend following (the square root of) Eq. (1) suggesting a saturated $u_p'^+ \approx 3.4$ as $\mathrm{Re}_\tau \to \infty$ [27]. Hence, different asymptotic states can be drawn for $u_p'^+$ as well. Incidentally, we note the data deviation of $u_p'^+$ for $\mathrm{Re}_\tau \leqslant 300$, which might be due to the transition history, e.g., the stable traveling wave effect in 2DCH. Moreover, for quasi-2D soap-film experiments, whether u_p' scales as U_b needs future verification when data become available.

IV. SUMMARY

In this work we have demonstrated glaring differences between 2D and 3D channel flows and explained their different asymptotic behaviors. These results provide a counterpart for the classical boundary layer perspective, that is, unbounded turbulent fluctuations in 2D wall flows induced by inverse cascade.

ACKNOWLEDGMENTS

APPENDIX A: NUMERICAL SETUP

We solve the incompressible 2D Navier–Stokes equations (with the density ρ absorbed into the pressure $\mathfrak{p}$),

$$\partial_t \mathfrak{u}_i + \partial_j \mathfrak{u}_i \mathfrak{u}_j = -\partial_i \mathfrak{p} + \nu \partial_j \partial_j \mathfrak{u}_i, \tag{A1}$$

$$\partial_i \mathfrak{u}_i = 0, \tag{A2}$$

using our own finite difference code which has been well validated for 3D channel (3DCH) flows [33]. Here x_i with indices $i = 1, 2$ represents the streamwise x and wall-normal y directions, respectively, and $\mathfrak{u}$, $\mathfrak{v}$ denote the instantaneous velocities in the respective directions (with

TABLE I. Parameters of the simulations. N_x is the number of grid cells in the streamwise direction and N_y is that in the wall-normal direction. Δx^+ and Δy^+ represent the grid spacings normalized by viscous units. T is the time interval for averaging, and U_b is the mean velocity. The first 16 cases correspond to the regular channel domain with $L_x = 8\delta$, and the last three cases correspond to the long channel domain with $L_x = 24\delta$. For all cases, $L_y = 2\delta$.

	Re_τ	$N_x \times N_y$	Δx^+	$\Delta y^+_{min} - \Delta y^+_{max}$	TU_b/δ
3000	127	1024×320	0.99	0.05–1.58	10 000
4000	157	1024×320	1.23	0.07–1.95	10 000
5000	187	1024×320	1.46	0.08–2.32	10 000
7000	248	2048×512	0.97	0.05–2.03	10 000
10 000	331	2048×512	1.29	0.07–2.70	10 000
15 000	419	2048×640	1.64	0.06–2.76	10 000
20 000	543	2048×640	2.12	0.08–3.58	10 000
30 000	662	2048×1024	2.59	0.06–2.70	15 000
50 000	952	2048×1024	3.72	0.09–3.88	15 000
70 000	1266	4096×2048	2.47	0.08–2.46	4000
100 000	1723	4096×2048	3.37	0.11–3.35	4000
150 000	2269	4096×2048	4.43	0.14–4.41	4000
200 000	2841	4096×2048	5.55	0.18–5.52	4000
300 000	3654	4096×2560	7.14	0.14–6.03	4000
500 000	5004	6144×3072	6.52	0.21–6.48	4000
1 000 000	8062	6144×3072	10.50	0.34–10.44	4000
3000	121	3072×320	0.95	0.05–1.51	5000
10 000	328	4096×512	1.92	0.07–2.67	5000
50 000	963	4096×1024	5.64	0.09–3.93	5000

a double index indicating summation). The simulation is in the domain $0 < y < L_y = 2\delta$ and $0 < x < L_x = 8\delta$ for regular cases and $0 < x < L_x = 24\delta$ for long cases, with periodic boundary conditions in the x direction and no-slip boundary conditions at both the top and bottom walls, where δ is the half-channel height. A second-order centered finite difference method with staggered grids is used for spatial discretization, and the second-order Runge-Kutta scheme is employed for time advancement. Fast Fourier transforms are employed to solve the pressure Poisson equation. The method used to sustain turbulence is based on a constant flow rate, while details on the parallelization and discretization are given in Ref. [33].

A summary of the simulations is shown in Table I. We performed 16 regular cases and three long cases with bulk Reynolds numbers (Re) ranging from 3×10^3 to 10^6, with the maximum Re being nearly five times larger than that reported in Ref. [26]. The corresponding friction Reynolds numbers (Re_τ) are from about 130 to 8100. Note that to align with 3D wall turbulence, we adopt the definitions of $Re = U_b\delta/\nu$ and $Re_\tau = u_\tau\delta/\nu$. These could be analytically converted into $Re_R = 3Re/2$ and $Re_{A,R} = 2\sqrt{2}Re_\tau$, where Re_R and $Re_{A,R}$ are the bulk and friction Reynolds numbers defined in Ref. [26], respectively.

The streamwise direction is discretized using a uniform grid, while the wall-normal direction employs a stretched grid for higher grid resolution near the walls. The grid spacing is shown in Table I. Due to the dimensionality reduction, simulations of 2D channels (2DCH) require a longer averaging time to obtain reliable data, as was also discussed in Refs. [25,26]. Our averaging time reaches $4000\delta/U_b$ for all cases, which is sufficiently long for data convergence. For the initial velocity fields, laminar Poiseuille solutions $U_0(y) = 6U_b(L_y - y)y/L_y^2$ with random perturbations are used for $Re_\tau \leqslant 543$, while for higher Re_τ, velocity fields at the closest lower Reynolds number are used to reduce simulation costs.

APPENDIX B: MOMENTUM BALANCE AND BUDGET EQUATION

We now present the derivation of the mean momentum balance equation in 2D pressure-driven channels. Averaging the streamwise momentum equation [$i = 1$ for Eq. (A1)] over time and streamwise ensembles, with an additional flip-over average with respect to the centerline,

$$\langle \phi \rangle(y) = \frac{1}{TL_x} \int_0^T \int_0^{L_x} \frac{\phi(y) + \phi(L_y - y)}{2} \, dt \, dx, \tag{B1}$$

yields

$$0 = \nu \frac{\partial^2 U}{\partial y^2} - \left\langle \frac{\partial \mathfrak{p}}{\partial x} \right\rangle - \frac{\partial \langle uv \rangle}{\partial y}. \tag{B2}$$

Here U is the mean streamwise velocity, and u, v is the fluctuating velocity (hereafter, lowercase letters represent fluctuations, capital letters represent average quantities, and the superscript prime indicates the RMS, consistent with the main text). Integrating Eq. (B2) for y from 0 to δ, we obtain the balance of the mean pressure gradient and wall shear stress,

$$-\left\langle \frac{\partial \mathfrak{p}}{\partial x} \right\rangle = \frac{u_\tau^2}{\delta}, \tag{B3}$$

where $u_\tau = \sqrt{\tau_w/\rho}$ is the friction velocity and $\tau_w = \mu \partial U/\partial y|_{y=0}$ is the mean wall shear stress.

Integrating Eq. (B2) again from 0 to y yields the momentum balance equation [23],

$$\nu \frac{\partial U}{\partial y} - \langle uv \rangle = u_\tau^2 \left(1 - \frac{y}{\delta}\right), \tag{B4}$$

where Eq. (B3) is substituted in. Normalizing the above equation using u_τ and ν/u_τ, we obtain Eq. (3), where $S^+ = \partial U^+/\partial y^+$ is the mean shear and $W^+ = -\langle uv \rangle^+$ is the Reynolds shear stress.

The budget equation of $\langle uu \rangle$ in a steady 2D channel is presented here following Ref. [3]:

$$\underbrace{-\langle uv \rangle \frac{\partial U}{\partial y}}_{P} + \underbrace{\frac{\nu}{2} \frac{\partial^2 \langle uu \rangle}{\partial y^2}}_{D} - \underbrace{\frac{1}{2} \frac{\partial \langle uuv \rangle}{\partial y}}_{N} + \underbrace{\left\langle p \frac{\partial u}{\partial x} \right\rangle}_{} = \underbrace{\nu \left\langle \frac{\partial u}{\partial x_k} \frac{\partial u}{\partial x_k} \right\rangle}_{\epsilon}. \tag{B5}$$

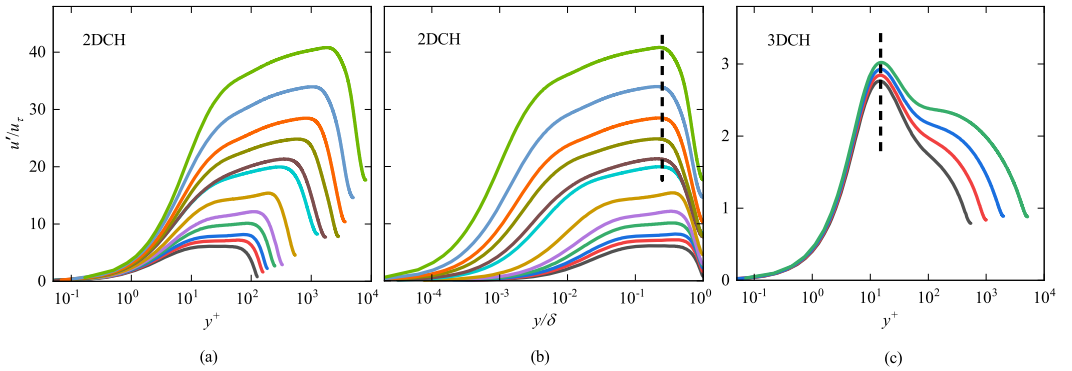FIG. 6. Streamwise velocity fluctuations in a 2D channel varying with (a) y^+ and (b) y/δ for Re_τ increasing from 130 to 8000 (from bottom to top). The dashed line in (b) represents $y/\delta = 0.25$. (c) Streamwise velocity fluctuations varying with y^+ in the 3D channels at $\mathrm{Re}_\tau = 550, 1000, 2000,$ and 5200 (from bottom to top), with the dashed line representing $y^+ = 15$. The 3D channel data are from Ref. [34].
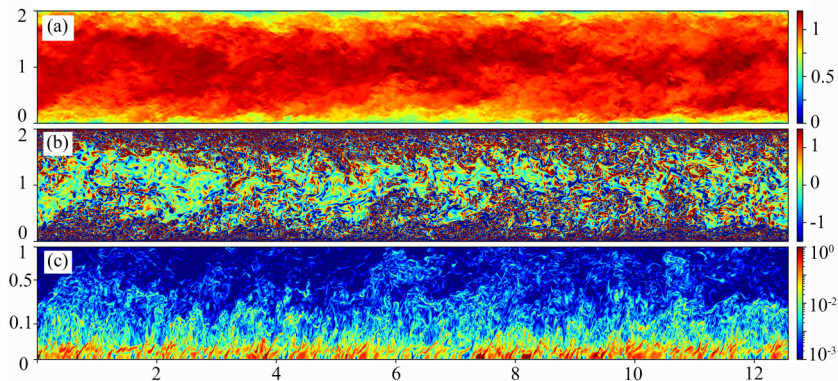
FIG. 7. Snapshots at the middle span ($z = L_z/2$) of 3DCH at $\mathrm{Re}_\tau = 2000$: (a) streamwise velocity; (b) vorticity; (c) turbulent dissipation rate. Abscissas are the same as in Fig. 2. Data are from our DNS of 3DCH [33].

Here P represents production, D the viscous diffusion, ϵ the dissipation, and N the nonlinear effect containing the pressure strain and turbulent transport. Normalizing the above equation by wall units yields Eq. (4).

Note that to compare with 3D channel data at a similar $\mathrm{Re}_\tau \approx 2000$, the case of the 2D channel in Fig. 4 actually corresponds to the case of $\mathrm{Re}_\tau = 1723$ in Table 1. The two Re_τ differ by about 10%, not affecting the conclusion drawn from the budget analysis.

APPENDIX C: STREAMWISE VELOCITY FLUCTUATIONS

As shown in Fig. 6, the wall-normal variations of the streamwise velocity fluctuations in the 2D and 3D channels are significantly different. For the 2D channel, the peak location varies according to $y^+ \approx 0.25\mathrm{Re}_\tau$ [Fig. 6(a)], which corresponds to $y/\delta \approx 0.25$ [the dashed line in Fig. 6(b)]. In contrast, the peak location in the 3D cases is fixed at about $y^+ = 15$ [the dashed line in Fig. 6(c)]. Therefore, the peak is an outer flow quantity in the 2D channel, as opposed to a near-wall quantity in the 3D channel [27,28].
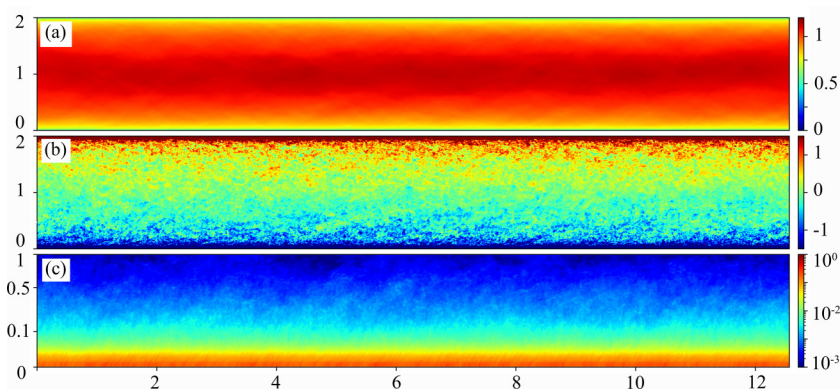

FIG. 8. The same plots as in Fig. 7 after spanwise averaging of the 3DCH at $\mathrm{Re}_\tau = 2000$.
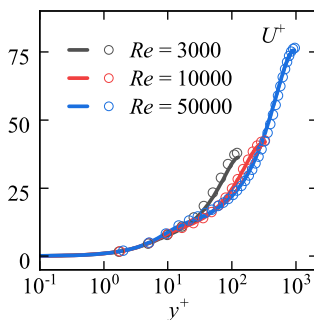
FIG. 9. Comparison of the streamwise mean velocity profiles between regular channels (lines) and long channels (circles) at the three Re values listed in Table 1.

APPENDIX D: DESCRIPTION OF MOVIES

Three movies labeled (a), (b), and (c) are included in the Supplemental Material [35]. In each movie, the three quantities displayed from top to bottom are the streamwise velocity, spanwise vorticity, and turbulent dissipation rate, respectively. Movie (a) shows the instantaneous fields of the 2DCH at $Re_\tau = 1723$, while Movie (b) shows the cross-sectional $(x - y)$ slice of the fields in the 3DCH at $Re_\tau = 2000$. Movie (c) shows the 3DCH result again after the spanwise averaging of Movie (b). Note that to generate 3DCH movies, we carried out another round of DNS at $Re_\tau = 2000$ using our own code, which was verified through comparison with the results of Ref. [34] in Ref. [33].

As explained in the main text, prominent large-scale wavy structures (LSWSs) are developed in the 2DCH, which are induced by antivortex pairs with extreme dissipation rates at the walls [see Movie (a) for a dynamic perspective]. As a comparison, Movie (b) and Fig. 7 show no such large-scale velocity or vortical structures dominating the 3DCH flow. Instead, small-scale structures are more developed and widely spread in 3DCH, which is unsurprising because of the vortex stretching and tilting effects. Moreover, Movie (c) and Fig. 8 show that after spanwise averaging, all three quantities in the 3DCH are layer-like distributed, in sharp contrast to the strong mixing seen for the 2DCH. This comparison clearly demonstrates that the inner-outer interactions are much less intensive in 3DCH than in 2DCH.

APPENDIX E: FLOWS IN LONG CHANNELS

In the main text, Fig. 1 and Fig. 5 show that the mean friction, the wall values of turbulent dissipation rate and pressure RMS, the bulk velocity, and the peak values of the streamwise velocity fluctuations are almost identical in regular and long channels. Here Fig. 9 further shows that the
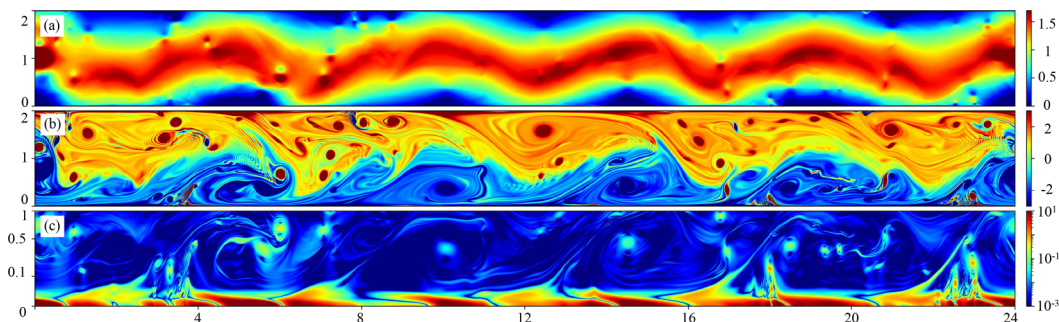

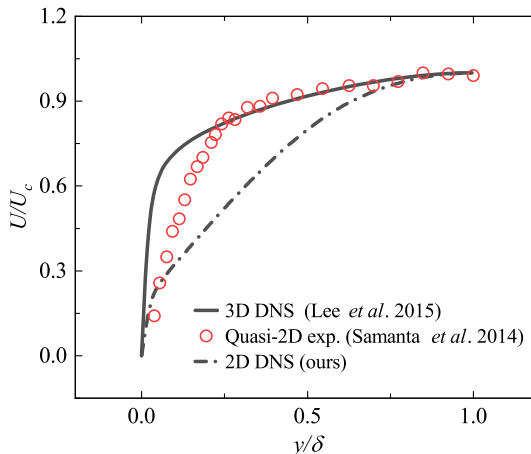FIG. 10. The same plots as in Fig. 7 but for long 2DCH at $Re_\tau = 963$.

FIG. 11. Mean velocity profiles in 3D (solid line), quasi-2D (circle), and 2D (dash-dotted line) channels. The data origins are marked in the legend. In particular, the mean velocity data of the quasi-2D soap-film experiments are from Fig. 2 of Ref. [24] at Re = 24 500 (the inverse energy cascade case).

mean velocity profiles are also identical between regular and long channels. Figure 10 also shows snapshots of the velocity, vorticity, and dissipation rate of the long channel at $\text{Re}_\tau = 963$. Again, the large-scale wavy structures are observed with wavelengths around 4.8δ, similar to what we found in Fig. 2.

APPENDIX F: COMPARISON WITH SOAP-FILM EXPERIMENTS

While both 2DCH and quasi-2D channels exhibit the 2D friction law, their mean velocity profiles are rather different. Figure 11 shows the mean velocity profiles in 3DCH, quasi-2D channel, and 2DCH. Profiles are displayed in outer units (i.e., U/U_c vs y/δ where U_c is the centerline velocity) so that the uncertainty of u_τ measurement is not an issue here. It is remarkable that in the bulk region ($y/\delta > 0.25$), the data of quasi-2D closely follow the trend of 3DCH, while near the wall, the quasi-2D result drops more slowly than the 3DCH result, with a trend more akin to the 2DCH case. It would be interesting to check whether the quasi-2D data are closer to the 2DCH case when the soap-film thickness is reduced. If so, the differences between 2DCH and soap-film experiments would be due to finite flow thickness in the latter case (although still a few microns as reported in [19]). Note that other issues, such as air drag and streamwise inhomogeneity, could also cause the differences between quasi-2D and 2D flows.

[1] K. Sreenivasan, The turbulent boundary layer, in *Frontiers in Experimental Fluid Mechanics*, edited by M. Gad-el-Hak (Springer, Berlin, 1989), pp. 159–209.

[2] U. Frisch, *Turbulence: The Legacy of A. N. Kolmogorov* (Cambridge University Press, Cambridge, 1995).

[3] S. B. Pope, *Turbulent Flows* (Cambridge University Press, Cambridge, 2000).

[4] B. J. McKeon and K. R. Sreenivasan, Introduction: scaling and structure in high Reynolds number wall-bounded flows, Philos. Trans. R. Soc. A **365**, 635 (2007).

[5] I. Marusic, B. J. McKeon, P. A. Monkewitz, H. M. Nagib, A. J. Smits, and K. R. Sreenivasan, Wall-bounded turbulent flows at high Reynolds numbers: Recent advances and key issues, Phys. Fluids **22**, 065103 (2010).

[6] A. J. Smits, B. J. McKeon, and I. Marusic, High-Reynolds number wall turbulence, Annu. Rev. Fluid Mech. **43**, 353 (2011).

[7] J. C. Klewicki, Bounded dissipation predicts finite asymptotic state of near-wall turbulence, J. Fluid Mech. **940**, F1 (2022).

[8] R. H. Kraichnan, Inertial ranges in two-dimensional turbulence, Phys. Fluids **10**, 1417 (1967).

[9] G. K. Batchelor, Computation of the energy spectrum in homogeneous two-dimensional turbulence, Phys. Fluids **12**, II-233 (1969).

[10] G. Boffetta and R. E. Ecke, Two-dimensional turbulence, Annu. Rev. Fluid Mech. **44**, 427 (2012).

[11] G. Falkovich, G. Boffetta, M. Shats, and A. Lanotte, Introduction to focus issue: Two-dimensional turbulence, Phys. Fluids **29**, 110901 (2017).

[12] S. Chen, R. E. Ecke, G. L. Eyink, M. Rivera, M. Wan, and Z. Xiao, Physical mechanism of the two-dimensional inverse energy cascade, Phys. Rev. Lett. **96**, 084502 (2006).

[13] N. Guttenberg and N. Goldenfeld, Friction factor of two-dimensional rough-boundary turbulent soap film flows, Phys. Rev. E **79**, 065306(R) (2009).

[14] G. Boffetta and S. Musacchio, Evidence for the double cascade scenario in two-dimensional turbulence, Phys. Rev. E **82**, 016307 (2010).

[15] P. Tabeling, Two-dimensional turbulence: A physicist approach, Phys. Rep. **362**, 1 (2002).

[16] H. Xia, H. Punzmann, G. Falkovich, and M. G. Shats, Turbulence-condensate interaction in two dimensions, Phys. Rev. Lett. **101**, 194504 (2008).

[17] H.-Y. Zhu, J.-H. Xie, and K.-Q. Xia, Circulation in quasi-2D turbulence: Experimental observation of the area rule and bifractality, Phys. Rev. Lett. **130**, 214001 (2023).

[18] H. Kellay, X.-I. Wu, and W. I. Goldburg, Experiments with turbulent soap films, Phys. Rev. Lett. **74**, 3975 (1995).

[19] H. Kellay and W. Goldburg, Two-dimensional turbulence: A review of some recent experiments, Rep. Prog. Phys. **65**, 845 (2002).

[20] T. Tran, P. Chakraborty, N. Guttenberg, A. Prescott, H. Kellay, W. Goldburg, N. Goldenfeld, and G. Gioia, Macroscopic effects of the spectral structure in turbulent flows, Nat. Phys. **6**, 438 (2010).

[21] H. Kellay, T. Tran, W. Goldburg, N. Goldenfeld, G. Gioia, and P. Chakraborty, Testing a missing spectral link in turbulence, Phys. Rev. Lett. **109**, 254502 (2012).

[22] A. Vilquin, J. Jagielka, S. Djambov, H. Herouard, P. Fischer, C.-H. Bruneau, P. Chakraborty, G. Gioia, and H. Kellay, Asymptotic turbulent friction in 2D rough-walled flows, Sci. Adv. **7**, eabc6234 (2021).

[23] V. S. L'vov, I. Procaccia, and O. Rudenko, Velocity and energy profiles in two- versus three-dimensional channels: Effects of an inverse- versus a direct-energy cascade, Phys. Rev. E **79**, 045304(R) (2009).

[24] D. Samanta, F. Ingremeau, R. Cerbus, T. Tran, W. I. Goldburg, P. Chakraborty, and H. Kellay, Scaling of near-wall flows in quasi-two-dimensional turbulent channels, Phys. Rev. Lett. **113**, 024504 (2014).

[25] V. K. Markeviciute and R. R. Kerswell, Degeneracy of turbulent states in two-dimensional channel flow, J. Fluid Mech. **917**, A57 (2021).

[26] G. Falkovich and N. Vladimirova, Turbulence appearance and nonappearance in thin fluid layers, Phys. Rev. Lett. **121**, 164501 (2018).

[27] X. Chen and K. R. Sreenivasan, Reynolds number scaling of the peak turbulence intensity in wall flows, J. Fluid Mech. **908**, R3 (2021).

[28] X. Chen and K. R. Sreenivasan, Law of bounded dissipation and its consequences in turbulent wall flows, J. Fluid Mech. **933**, A20 (2022).

[29] D. B. DeGraaff and J. K. Eaton, Reynolds-number scaling of the flat plate turbulent boundary layer, J. Fluid Mech. **422**, 319 (2000).

[30] I. Marusic, W. J. Baars, and N. Hutchins, Scaling of the streamwise turbulence intensity in the context of inner-outer interactions in wall turbulence, Phys. Rev. Fluids **2**, 100502 (2017).

[31] P. Monkewitz, Asymptotics of streamwise Reynolds stress in wall turbulence, J. Fluid Mech. **931**, A18 (2022).

[32] H. Nagib, P. Monkewitz, and K. Sreenivasan, Reynolds number required to accurately discriminate between proposed trends of peak normal stress in wall turbulence, *75th Annual Meeting of the Division of Fluid Dynamics*, Indianapolis, Indiana (2022), https://meetings.aps.org/Meeting/DFD22/Session/Q13.6.

[33] J. Xie, J. He, Y. Bao, and X. Chen, A low-communication-overhead parallel DNS method for the 3D incompressible wall turbulence, Intl. J. Comput. Fluid Dyn. **35**, 413 (2021).

[34] M. Lee and R. D. Moser, Direct numerical simulation of turbulent channel flow up to $Re_\tau \approx 5200$, J. Fluid Mech. **774**, 395 (2015).

[35] See Supplemental Material at http://link.aps.org/supplemental/10.1103/PhysRevFluids.9.034609 for movies of the structural comparisons between 2D and 3D channels at similar $Re_\tau \approx 2000$.

[36] I. Marusic, R. Mathis, and N. Hutchins, Predictive model for wall-bounded turbulent flow, Science **329**, 193 (2010).

[37] H. M. Nagib, K. A. Chauhan, and P. A. Monkewitz, Approach to an asymptotic state for zero pressure gradient turbulent boundary layers, Philos. Trans. R. Soc. A **365**, 755 (2007).

[38] M. Chertkov, C. Connaughton, I. Kolokolov, and V. Lebedev, Dynamics of energy condensation in two-dimensional turbulence, Phys. Rev. Lett. **99**, 084501 (2007).

[39] H. Xia, M. Shats, and G. Falkovich, Spectrally condensed turbulence in thin layers, Phys. Fluids **21**, 125101 (2009).

[40] N. Francois, H. Xia, H. Punzmann, and M. Shats, Inverse energy cascade and emergence of large coherent vortices in turbulence driven by Faraday waves, Phys. Rev. Lett. **110**, 194501 (2013).

[41] R. H. Kraichnan and D. Montgomery, Two-dimensional turbulence, Rep. Prog. Phys. **43**, 547 (1980).

[42] S. Chen, R. E. Ecke, G. L. Eyink, X. Wang, and Z. Xiao, Physical mechanism of the two-dimensional enstrophy cascade, Phys. Rev. Lett. **91**, 214501 (2003).

[43] C.-C. Liu, R. T. Cerbus, and P. Chakraborty, Janus spectra in two-dimensional flows, Phys. Rev. Lett. **117**, 114502 (2016).

[44] Note that $t_w \sim \delta/U_b$ is not considered as it leads to vanishing ϵ_w^+ towards high Re_τ; moreover, as viscosity is necessary for dissipation, we have $t_w \sim \ell_\tau/U_b$.